Research Square

Preprints are preliminary reports that have not undergone peer review.
They should not be considered conclusive, used to inform clinical practice,
or referenced by the media as validated information.

Physics-Informed Neural Networks for solving 2D Shallow Water Equations: Accuracy Assessment Through Dambreak Benchmark Problems

Abdelkader Bemmoussat
Djillali Liabes University of Sidi Bel Abbes
Noureddine Maref
Djillali Liabes University of Sidi Bel Abbes
Zakaria Mahfoud
Djillali Liabes University of Sidi Bel Abbes
Khaled Korichi
kh.korichi@gmail.com
Djillali Liabes University of Sidi Bel Abbes

Research Article

Keywords: Physics-Informed Neural Networks (PINNs), Shallow Water Equations, Dambreak flow simulation, Wet–dry front propagation, Experimental data, Accuracy assessment

Posted Date: July 24th, 2026

DOI: https://doi.org/10.21203/rs.3.rs-10097604/v1

License: This work is licensed under a Creative Commons Attribution 4.0 International License.
Read Full License

Additional Declarations: No competing interests reported.

Physics-Informed Neural Networks for solving 2D Shallow Water Equations: Accuracy Assessment Through Dambreak Benchmark Problems

Dr. Abdelkader Bemmoussat
Email: abdelkader.bemmoussat@univ-sba.dz
ORCID: https://orcid.org/0000-0002-8110-2054
Laboratory of Civil Engineering and Environment, Faculty of Technology, Djillali Liabes University of Sidi Bel Abbes, BP 89 Sidi Bel Abbes 22000, Algeria

Dr. Noureddine Maref
Email: noureddine.maref@univ-sba.dz
ORCID: https://orcid.org/0000-0001-8640-7319
Laboratory of Civil Engineering and Environment, Faculty of Technology, Djillali Liabes University of Sidi Bel Abbes, BP 89 Sidi Bel Abbes 22000, Algeria

Dr. Zakaria Mahfoud
Email: zakaria.mahfoud@univ-sba.dz
ORCID: https://orcid.org/0000-0003-3168-7792
Laboratory of Civil Engineering and Environment, Faculty of Technology, Djillali Liabes University of Sidi Bel Abbes, BP 89 Sidi Bel Abbes 22000, Algeria

Prof. Khaled Korichi (*Corresponding author)
Email: kh.korichi@gmail.com, Tel : 213791563124
ORCID: https://orcid.org/0000-0002-2663-2757
Laboratory of Civil Engineering and Environment, Faculty of Technology, Djillali Liabes University of Sidi Bel Abbes, BP 89 Sidi Bel Abbes 22000, Algeria

Abstract

This paper evaluates a unified Physics-Informed Neural Network (PINN) framework for simulating dam-break flows governed by the two-dimensional shallow water equations (SWEs). By embedding the continuity and momentum equations directly into the loss function via automatic differentiation, the framework enforces physical consistency without a computational mesh. Four benchmark cases of increasing complexity are considered: a canonical 1D dam-break over wet and dry beds, a 1D dam-break over a triangular hump with transcritical flow and hydraulic jump formation, a 2D partial dam-break with lateral spreading, and a 2D dam-break through a Venturi channel. Predictions are assessed against analytical solutions and experimental measurements. Across all configurations, the model achieves R^2 values between 0.982 and 0.997, RMSE below 0.01 m, and L2 errors within engineering tolerances. The mesh-free approach proves especially well-suited to geometrically complex domains, positioning PINNs as a practical surrogate for finite-volume solvers in rapid flood risk assessment.

Keywords Physics-Informed Neural Networks (PINNs), Shallow Water Equations, Dambreak flow simulation, Wet–dry front propagation, Experimental data, Accuracy assessment.

Introduction

Accurate simulation of free-surface flows underpins a wide range of engineering and environmental problems, from flood inundation mapping and dam-break wave propagation to tsunami run-up and tidal dynamics in estuaries. In all these settings, practitioners need tools that resolve rapidly varying flow regimes, supercritical–subcritical transitions, moving wet–dry fronts, and bed-induced hydraulic jumps, without prohibitive computational cost. The shallow water equations (SWEs), or Saint–Venant equations in 1D, are the standard mathematical framework for this class of problems. Derived by depth-averaging the Navier–Stokes equations under the hydrostatic pressure assumption, they govern the evolution of water depth and velocity across a broad range of geophysical and engineering scales (Toro, 2001; Vreugdenhil, 2013). Their mathematical structure, a system of nonlinear hyperbolic conservation laws with with bed-slope and friction source terms that capture the essential physics of shallow free-surface flows.

Three discretisation paradigms have been applied to the SWEs: FDM, FEM, and FVM. FDM is simple to implement on structured grids but handles irregular boundaries poorly (Strikwerda, 2004). FEM offers geometric flexibility and high-order approximations but incurs heavy matrix-assembly overhead for transient problems (Zienkiewicz & Taylor, 2005). FVM dominates contemporary computational hydraulics because it enforces conservation of mass and momentum at the discrete cell level and handles flow discontinuities through Riemann-solver fluxes (Toro, 2001). High-resolution Godunov-type schemes, including the Roe approximate Riemann solver (Roe, 1981), the HLLE scheme (Harten et al., 1983), and the HLLC solver (Toro et al., 1994) have proven effective at capturing shocks, rarefaction waves, and wet–dry interfaces in dam-break flows. Operational platforms such as HEC-RAS 2D (Brunner, 2016), which employs an implicit FVM formulation on unstructured grids, and LISFLOOD-FP (Bates et al., 2010), which uses an explicit finite-difference inertial scheme on raster grids, represent the current state of practice.

Classical grid-based solvers, despite their maturity, share several structural limitations. Mesh generation for geometrically complex or dynamically evolving domains remains time-consuming and error-prone (Thompson et al., 1998). Resolving sharp flow features requires fine grids that drive up memory and runtime. Explicit schemes are constrained by the CFL stability condition (LeVeque, 2002), which links the allowable time step to grid resolution and wave speed, a hard constraint for large-scale, fine-resolution runs. Taken together, these bottlenecks are most felt in operational flood forecasting, where speed and limited computing resources demand leaner alternatives.

Machine learning (ML) has been increasingly adopted in water sciences as computing power and high-resolution remote sensing data have become widely available. Early efforts used ANNs, support vector machines, and ensemble methods as surrogates for expensive hydrodynamic models (Solomatine & Ostfeld, 2008); (Bermúdez et al., 2019). Convolutional neural networks (CNNs) and LSTM architectures subsequently extended these capabilities to flood forecasting, inundation mapping, and spatiotemporal flow prediction (Guo et al., 2021; Hu et al., 2019). Zhang et al. (2020) demonstrated that CNN-based emulators can predict 2D flood inundation patterns at speeds several orders of magnitude faster than conventional FVM solvers, making real-time ensemble forecasting feasible. Similarly, machine learning-driven emulators for open-source flood models using convolutional LSTM architectures have been developed to capture the spatiotemporal dynamics of flood events at basin scale (Kabir et al., 2020).

Purely data-driven models, however, have well-known limitations: they require large labelled datasets, offer no guarantee of satisfying conservation laws, and extrapolate poorly outside

their training distribution. The absence of standardised benchmark datasets for ML model evaluation compounds these issues (Mosavi et al., 2018). These shortcomings have driven interest in physics-constrained learning architectures that embed governing equations directly into the training process.

Physics-Informed Neural Networks (PINNs), introduced by Raissi et al. (2019), directly address these weaknesses. A PINN trains a deep neural network to approximate a PDE solution by minimising a composite loss that combines residuals of the PDE, initial conditions, and boundary conditions at scattered collocation points. Partial derivatives are computed via automatic differentiation (Baydin et al., 2018), which avoids discretisation error entirely. No computational mesh is required; the governing physics themselves act as the regulariser.

The seminal contribution of Raissi et al. (2019) demonstrated PINN solutions for the Burgers equation, Schrödinger equation, and the Navier–Stokes equations, establishing the method's capacity for both forward simulation and inverse parameter identification. This work has since inspired a broad literature on PINN applications across fluid mechanics, solid mechanics, heat transfer, and geophysics. Karniadakis et al. (Karniadakis et al., 2021) provided a comprehensive review of physics-informed learning, positioning PINNs within the broader landscape of scientific machine learning and outlining key open challenges including training stability, convergence for multi-scale problems, and computational efficiency.

Several important methodological advances have followed. Jagtap et al. (2020) introduced extended PINNs (XPINNs) employing domain decomposition, significantly improving training efficiency for large-scale and geometrically complex problems by partitioning the domain into subdomains, each trained with a local network subject to interface continuity conditions. Meng et al. (2019) proposed parallel PINNs (ppPINNs) leveraging multi-GPU architectures to further accelerate training on decomposed domains. Bihlo and Popovych (2022) studied adaptive activation functions for advection-dominated and hyperbolic equations, demonstrating that learnable activation parameters improve solution sharpness near discontinuities. Xu and Darve (2019) proposed adaptive residual-based collocation sampling strategies that concentrate training points in regions of high PDE residual, substantially improving convergence for problems with localised steep gradients—a feature directly relevant to Dambreak fronts. The challenge of balancing multiple loss terms, which is particularly acute in the SWEs where continuity and momentum residuals operate on different physical scales, has been addressed through automatic loss weighting strategies. The NDAWL-PINN framework (Nascimento et al., 2020) employs a non-dimensionalisation method combined with an automatic weighted loss algorithm, making the training process less sensitive to manual hyperparameter tuning.

The application of PINNs to the SWEs has emerged as an active research frontier, motivated by the potential for mesh-free, data-sparse simulation of hydraulic flows. Early contributions addressed simplified or steady-state formulations. Cedillo et al. (2022) applied PINNs to one-dimensional steady-state river flow, performing dimensional transformation on the energy differential equation, a steady-state simplification of the SWEs, and demonstrating that the method can effectively simulate subcritical and supercritical flow states in complex riverbeds. Tartakovsky et al. (2020) demonstrated PINNs for subsurface hydraulic conductivity identification, highlighting their flexibility for joint inversion problems where both the solution field and governing parameters are unknown simultaneously.

For transient 1D Dambreak problems, Qi et al. (2023) demonstrated accurate PINN recovery of water depth and velocity profiles under both wet-bed and dry-bed initial conditions, underscoring the importance of residual point sampling near the discontinuity and adaptive loss weighting to balance shock-region penalties against smoother flow regions. Feng et al. (2023)

embedded PINNs into the sub-grid of conventional numerical schemes, incorporating observational data to enhance the accuracy of river flow predictions, suggesting a hybrid approach that exploits the complementary strengths of both paradigms.

The treatment of variable bathymetry, essential for realistic modelling of river channels, floodplains, and coastal regions, poses additional challenges for PINNs because the bed slope source term introduces an imbalance between flux gradients and source terms that must be carefully handled to avoid spurious oscillations. Chen et al. (2020) incorporated bed elevation source terms directly into the PINN loss function and validated their approach on flow over smooth and discontinuous bed profiles, providing a framework directly relevant to the transcritical flow benchmark considered in the present study. Dazzi (2024) extended this approach by treating bed elevation as an additional conserved variable in an augmented SWE system, enabling the network to learn topographic information through automatic differentiation without requiring explicit specification of bed slope derivatives. This formulation is conceptually elegant but introduces additional unknowns and training complexity.

Two-dimensional extensions of PINNs for SWEs represent the current frontier of the field. Leiteritz et al. (2021) explored the effectiveness of different optimisers in PINNs applied to the radial Dambreak problem without topography, demonstrating accuracy comparable to traditional numerical methods in idealised symmetric configurations. Tian et al. (2025) employed both fully connected and convolutional neural network architectures to solve the 2D SWEs and applied these models to a real river basin, reporting simulation results comparable to those obtained with a finite volume solver. The authors addressed the most challenging configuration to date: 2D SWEs with rainfall source terms and complex topography. Through systematic theoretical analysis and experimental validation, they demonstrated that a hybrid variable-conservation formulation offers superior training performance, and importantly found that incorporating the energy conservation law as an entropy condition does not yield consistent improvement and may induce training failure, a practically significant negative result for PINN design. Bihlo and Popovych (2022) investigated PINNs for SWEs on spherical surfaces in the context of global atmospheric modelling, proposing to train sequences of networks over successive time intervals to address the well-known challenge of PINN accuracy degradation over long integration windows.

The literature reviewed above reveals a clear gap. PINNs have been applied to isolated shallow-water problems, specific 1D configurations, particular 2D geometries, or individual source-term treatments, but no study has systematically validated a single, unified framework across the canonical SWE benchmark suite under consistent architectural and training conditions. In particular, no published work has simultaneously addressed the 1D wet-bed and dry-bed dam-break, transcritical flow over a triangular bump, and the 2D partial dam-break. These four cases collectively test shock-capturing, wet–dry front propagation, bed source-term balance, and multi-dimensional wave dynamics. The step from 1D to 2D also introduces additional complexity for PINNs, more state variables, stronger nonlinear coupling, higher-dimensional collocation domains, yet this transition has not been studied in a controlled comparative framework.

This study addresses the identified gap by proposing and rigorously evaluating a unified PINN framework for both the 1D and 2D SWEs. The specific objectives of this work are threefold:

1. To formulate a PINN framework adapted to the 1D and 2D SWEs, incorporating bathymetric source terms, with detailed specification of the network architecture, loss function composition, collocation strategy, and training procedure;

2. To validate the framework against three canonical benchmarks of increasing complexity—the 1D Dambreak under wet and dry bed conditions, the 1D Dambreak over a triangular bump with transcritical flow, and the 2D partial Dambreak—using reference analytical solutions and high-resolution FVM results;
3. To assess systematically the accuracy, mesh-free flexibility, and current limitations of PINNs for hydraulic flow simulation, with particular attention to discontinuity resolution, dry-front dynamics, bathymetric source term treatment, and two-dimensional flow spreading, providing practical guidance for future applications in computational hydraulics.

2. Materials and Methods

2.1 2D Governing SWE Equations

The two-dimensional shallow water equations (SWEs) are derived from the depth-averaged Reynolds-averaged Navier–Stokes equations, assuming a hydrostatic pressure distribution, small bed slope, and negligible vertical accelerations. They represent a system of nonlinear, time-dependent, hyperbolic partial differential equations (PDEs) that describe water depth and horizontal momentum in free-surface flows. In conservative form, the 2D SWEs are written as:

$$\frac{\partial \boldsymbol{U}}{\partial \boldsymbol{t}} + \frac{\partial \boldsymbol{F}(\boldsymbol{U})}{\partial \boldsymbol{x}} + \frac{\partial \boldsymbol{G}(\boldsymbol{U})}{\partial \boldsymbol{y}} = \boldsymbol{S}(\boldsymbol{U}, \boldsymbol{x}, \boldsymbol{y}) \tag{1}$$

where the vector of conserved variables U, flux vectors F and G, and source vector S are defined as:

$$\boldsymbol{U} = [\boldsymbol{h}, \boldsymbol{hu}, \boldsymbol{hv}]^{\mathbf{T}} \tag{2}$$

$$\boldsymbol{F} = [\boldsymbol{hu}, \boldsymbol{hu}^2 + \boldsymbol{gh}^2/2, \boldsymbol{huv}]^{\mathbf{T}} \tag{3}$$

$$\boldsymbol{G} = [\boldsymbol{hv}, \boldsymbol{huv}, \boldsymbol{hv}^2 + \boldsymbol{gh}^2/2]^{\mathbf{T}} \tag{4}$$

$$\boldsymbol{S} = [\mathbf{0}, \boldsymbol{gh}(\boldsymbol{S_{0x}} - \boldsymbol{S_{fx}}), \boldsymbol{gh}(\boldsymbol{S_{0y}} - \boldsymbol{S_{fy}})]^{\mathbf{T}} \tag{5}$$

Here, h(x, y, t) [m] is the water depth; u(x, y, t) and v(x, y, t) [m/s] are the depth-averaged velocity components in the x- and y-directions, respectively; g = 9.81 m/s² is gravitational acceleration; z^b(x, y) [m] is the bed elevation; $S_0x = -\partial z^b/\partial x$ and $S_0y = -\partial z^b/\partial y$ are the corresponding x and y bed slopes respectively. The friction slopes Sfx and Sfy are computed using the Manning–Strickler formula:

$$\boldsymbol{S_{fx}} = \frac{\boldsymbol{n}^2\boldsymbol{u}\sqrt{\boldsymbol{u}^2+\boldsymbol{v}^2}}{\boldsymbol{h}^{4/3}}, \quad \boldsymbol{S_{fy}} = \frac{\boldsymbol{n}^2\boldsymbol{v}\sqrt{\boldsymbol{u}^2+\boldsymbol{v}^2}}{\boldsymbol{h}^{4/3}} \tag{6}$$

where n is the Manning roughness coefficient. Friction source terms may be omitted for idealised benchmark configurations; their inclusion within the PINN framework is straightforward by appending the friction terms to S.

From a physical standpoint, the SWEs are the depth-averaged form of the Navier–Stokes equations under the hydrostatic pressure assumption; mathematically, they form a hyperbolic system of PDEs.

2.2 Physics-Informed Neural Networks

A PINN embeds physical laws; PDEs, boundary conditions (BCs), and initial conditions (ICs), directly into the neural network training process, reducing or eliminating the need for labelled data and expensive numerical simulations.

The key idea is to approximate the solution variables h(x, y, t), u(x, y, t), and v(x, y, t) by a deep neural network N_θ parametrised by trainable weights and biases θ, which takes as input the spatial-temporal coordinates ξ = (x, y, t) and produces as output an approximation of the solution vector:

$$\widehat{\boldsymbol{U}}(\boldsymbol{x},\boldsymbol{y},\boldsymbol{t}) = \boldsymbol{N}_{\boldsymbol{\theta}}(\boldsymbol{x},\boldsymbol{y},\boldsymbol{t}) \approx [\boldsymbol{h},\boldsymbol{hu},\boldsymbol{hv}] \tag{7}$$

Unlike conventional data-driven neural networks, PINNs exploit automatic differentiation to compute exact partial derivatives of the network output with respect to its inputs. These derivatives are used to evaluate the PDE residuals at a set of collocation points distributed throughout the space-time domain, and the residuals are incorporated into the loss function. Training a data-free PINN (i.e., when labelled input–output data are not used) requires the network to satisfy the governing PDEs, ICs, and BCs simultaneously.

2.2.1 Neural Network Architecture

The network architecture consists of L fully connected (dense) hidden layers, each containing N neurons. The input layer accepts the coordinates (x, y, t) and the output layer produces the three predicted quantities ($\hat{h}$, $\hat{hu}$, $\hat{hv}$). Each hidden layer employs the conventional hyperbolic tangent (tanh) activation function:

$$\boldsymbol{\sigma}(\boldsymbol{z}) = \mathbf{tanh}(\boldsymbol{z}) \tag{8}$$

The tanh activation is selected for its smooth, differentiable character and its effectiveness in PINN applications (Raissi et al., 2019). The full network function is:

$$\boldsymbol{N}_{\boldsymbol{\theta}}(\boldsymbol{\xi}) = \boldsymbol{W}_{\boldsymbol{L}}\boldsymbol{\sigma}(\cdots \boldsymbol{\sigma}(\boldsymbol{W}_{\boldsymbol{2}}\boldsymbol{\sigma}(\boldsymbol{W}_{\boldsymbol{1}}\boldsymbol{\xi} + \boldsymbol{b}_{\boldsymbol{1}}) + \boldsymbol{b}_{\boldsymbol{2}})\cdots) + \boldsymbol{b}_{\boldsymbol{L}} \tag{9}$$

where W_l and b_l denote the weight matrix and bias vector of layer 1, respectively. Input and output features are normalised to the range [−1, 1] to improve training stability (Cai et al., 2022).

Following Tian et al. (2025), every sub-network receives the same raw inputs so that the trainable parameters for each output variable are decoupled. This significantly improves prediction accuracy in multivariate problems, particularly when the distributions and magnitudes of the output variables differ substantially.

2.2.2 Loss Function Formulation

The PINN is trained by minimising a composite loss function that incorporates physical constraints, initial conditions, boundary conditions, and (optionally) sparse data:

$$\boldsymbol{L}_{\mathbf{total}}(\boldsymbol{\theta}) = \boldsymbol{w}_{\mathbf{pde}} \cdot \boldsymbol{L}_{\mathbf{pde}} + \boldsymbol{w}_{\mathbf{ic}} \cdot \boldsymbol{L}_{\mathbf{ic}} + \boldsymbol{w}_{\mathbf{bc}} \cdot \boldsymbol{L}_{\mathbf{bc}} + \boldsymbol{w}_{\mathbf{data}} \cdot \boldsymbol{L}_{\mathbf{data}} \tag{10}$$

Each component is defined as a mean squared error (MSE) over dedicated sets of collocation or training points:

PDE residual loss: enforces the governing equations at N_{pde} interior collocation points $\{(x_i, y_i, t_i)\}_{i=1}^{Npde}$.

$$\boldsymbol{L}_{\mathbf{pde}} = \frac{\mathbf{1}}{\boldsymbol{N}_{\mathbf{pde}}} \sum_{\boldsymbol{i}} \|\boldsymbol{R}(\widehat{\boldsymbol{U}}(\boldsymbol{\xi}_{\boldsymbol{i}};\boldsymbol{\theta}))\|^{\mathbf{2}} \tag{11}$$

where $R(\cdot)$ is the PDE residual operator evaluated via automatic differentiation, encompassing residuals of the continuity (R_h), x-momentum (R_{hu}), and y-momentum (R_{hv}) equations.

IC residual loss: enforces initial conditions at N_{ic} points:

$$\boldsymbol{L_{ic}} = \frac{\mathbf{1}}{\boldsymbol{N_{ic}}} \sum_{\boldsymbol{i}} \|\widehat{\boldsymbol{U}}(\boldsymbol{x_i}, \mathbf{t} = \mathbf{0};\ \boldsymbol{\theta}) - \boldsymbol{U_0}(\boldsymbol{x_i})\|^2 \tag{12}$$

BC residual loss: enforces boundary conditions at N_{bc} boundary points:

$$\boldsymbol{L_{bc}} = \frac{\mathbf{1}}{\boldsymbol{N_{bc}}} \sum_{\boldsymbol{i}} \|\boldsymbol{B}\left(\widehat{\boldsymbol{U}}(\boldsymbol{x_i}; \boldsymbol{\theta})\right) - \boldsymbol{g}(\boldsymbol{x_i})\|^2 \tag{13}$$

where U_0 represents the initial condition and $B(\cdot) = g(\cdot)$ encodes the boundary conditions. The weights w_{pde}, w_{ic}, w_{bc}, and w_{data} are hyper-parameters controlling the relative importance of each constraint. Their values are tuned empirically for each benchmark case. Approaches such as NDAWL-PINN, which employs an Automatic Weighted Loss algorithm with a loss-term non-dimensionalisation method, have been proposed to reduce the manual effort in weight adjustment (Tian et al., 2025).

2.2.3 Training Strategy and Optimisation

Training is performed in two sequential phases following the approach of Raissi et al. (2019) and Qi et al. (2023):

Global exploration: The Adam optimiser (Kingma & Ba, 2014) is used with an initial learning rate of 10^{-3}, decayed by a factor of 0.9 every 2,000 iterations, for a total of 20,000–50,000 epochs. This phase rapidly reduces the loss to a neighbourhood of the minimum.

Local refinement: The Limited-memory Broyden–Fletcher–Goldfarb–Shanno (L-BFGS) algorithm is applied to fine-tune the network weights until convergence to a tighter tolerance. L-BFGS exploits second-order curvature information and typically achieves near machine-precision residuals within a few hundred iterations.

Collocation points for L_{pde} are sampled using Latin Hypercube Sampling (LHS) over the space-time domain to ensure a uniform and space-filling distribution (Xu & Darve, 2019). Adaptive resampling is applied every 5,000 Adam iterations, concentrating additional points in regions where the PDE residual exceeds a prescribed threshold. This strategy is critical for problems involving shocks and steep gradients.

2.2.5 Methodology Flowchart

Figure 1 summarises the step-by-step PINN methodology applied to the two-dimensional shallow water equations.

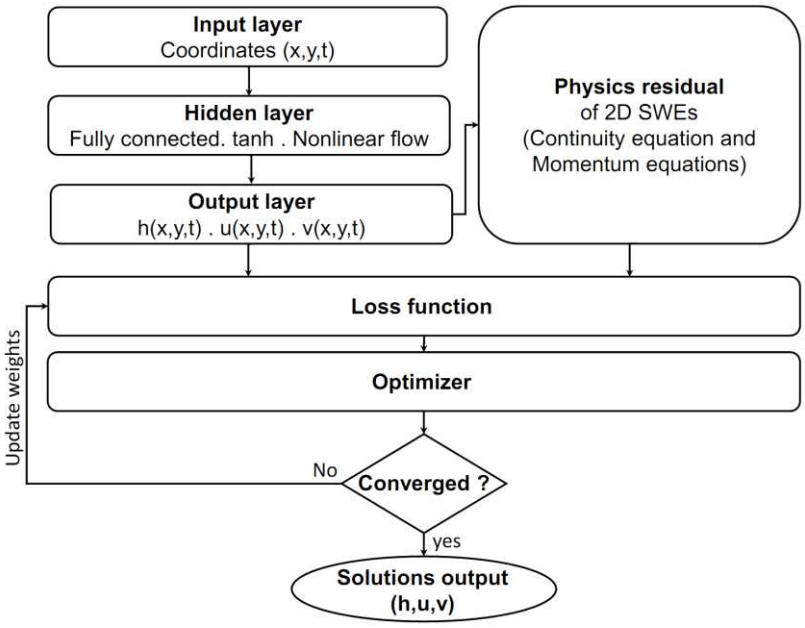


Figure 1. PINN framework flowchart for the 2D shallow water.

2.3 Benchmark Test Cases

To systematically assess the accuracy and robustness of the proposed PINN framework, five benchmark Dambreak test cases of increasing complexity are considered. These problems are characterised by highly unsteady, transient flow conditions in which the flow variables, water depth h and depth-averaged velocity components u and v, vary rapidly in both space and time. Together, they cover a broad spectrum of physical and numerical challenges relevant to shallow water modelling.

The selection criteria for these benchmark cases are as follows: (i) the flows are genuinely unsteady and transient; (ii) the solutions contain shock waves and rarefaction waves arising from the highly nonlinear character of the SWEs; (iii) wet/dry front propagation is present in several cases, requiring robust treatment of near-zero water depths; and (iv) the bed topography varies in one or both horizontal directions in the more complex cases, activating the source terms of the governing equations. For all test cases, numerical predictions are validated against either exact analytical solutions or published laboratory experimental data, providing a rigorous and unambiguous basis for performance evaluation. Table 1 summarises the key characteristics of each benchmark case.

Table 1. Summary of benchmark test case characteristics.

Test Case	Reference Data	1D/2D	Source Terms	Hydraulic Jump	Topographic Variation
1D Ideal Dambreak	Analytical	1D	No	Yes	None
Triangular Hump	Experimental	1D	Yes	Yes	Bathymetry
Partial Dambreak	Experimental	2D	No	No	None
Venturi Channel	Experimental	2D	Yes	Yes	Horizontal

2.3.1 1D Ideal Dambreak over Wet and Dry Beds

This classical benchmark problem is widely used to verify the ability of numerical schemes to capture shock waves and rarefaction fans in the context of the one-dimensional SWEs. The exact analytical solution is given by Gallardo et al. (2007) and provides a definitive reference for assessing numerical accuracy in the presence of discontinuities.

The configuration consists of a smooth, horizontal, frictionless rectangular channel of width b = 10 m and length L = 200 m. The dam is located at x = 100 m. The initial velocity is zero throughout the domain, and the initial water depth is defined by a step function across the dam location. Two sub-cases are investigated:

Wet-bed case: h(x, 0) = 10 m if x ≤ 100 m, h(x, 0) = 5 m if x > 100 m

Dry-bed case: h(x, 0) = 10 m if x ≤ 100 m, h(x, 0) = 0 m if x > 100 m

In the wet-bed case, the downstream water depth is non-zero, producing both a rightward-propagating shock wave and a leftward-propagating rarefaction fan. In the dry-bed case, the downstream domain is initially empty, resulting in a rarefaction wave and a dry-front advancing into the initially dry region. Open (transmissive) boundary conditions are applied at both the upstream and downstream ends of the channel.

2.3.2 1D Dambreak over a Triangular Hump

This benchmark investigates the interaction of a Dambreak wave with a triangular obstacle and was conducted at the Université Libre de Bruxelles, Belgium, as part of the European Commission's CADAM project (Morris, 2000). It is specifically designed to test the ability of numerical schemes to handle spatially varying bed topography, wet/dry fronts, and the formation of hydraulic jumps. The accuracy and stability of the scheme in the vicinity of the topographic obstacle are of particular interest.

The physical model is a 38 m long, 0.75 m wide horizontal channel (Figure 2). A dam located at x = 15.5 m separates the upstream reservoir, initially filled to a depth of 0.75 m, from the downstream floodplain, which is initially dry except for a region immediately downstream of the triangular hump where the water depth is maintained at 0.15 m. The triangular obstacle has a height of 0.4 m and a base length of 6.0 m, with its apex located 13 m downstream of the dam. Closed-wall boundary conditions are applied at both ends of the channel. The Manning roughness coefficient is n = 0.0125 $m^{-1/3}s$ and the total simulation time is 90 s.

Six gauge points (G4, G10, G13, G14, G15, and G20) are installed at 4, 10, 13, 14, 15, and 20 m downstream of the dam, respectively, providing time series of water depth for model validation.

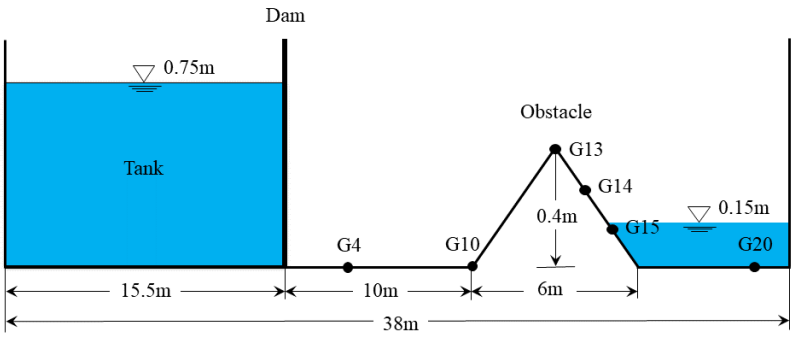


Figure 2. Schematic of the Dambreak over a triangular hump.

2.3.2 Two-Dimensional Partial Dambreak

This benchmark is based on the laboratory experiment of Fraccarollo and Toro (1995), which has become a standard reference for validating 2D shallow water solvers in the presence of shock waves and wet/dry interfaces. The experiment reproduces a realistic partial Dambreak scenario with a finite-width breach, enabling assessment of the model's performance under two-dimensional, highly transient conditions.

The computational domain consists of a reservoir of dimensions 1 m × 2 m connected through a 0.4 m wide centrally located breach to a downstream floodplain of dimensions 3 m × 2 m (Figure 3). The three outer boundaries of the floodplain are treated as open (transmissive) conditions. The initial water depth in the reservoir is $h_0 = 0.6$ m, while the floodplain is initially dry. The channel bed is horizontal and frictionless throughout.

Water surface elevation hydrographs are recorded at nine gauge points distributed across the domain. The coordinates of these gauges are listed in Table 2, and their spatial arrangement is illustrated in Figure 3.

Table 2. Coordinates of gauge points for the partial Dambreak test case.

Gauge	-5A	-4B	C	O	4	4A	8A	10A	5B
X (m)	0.18	0.15	0.48	1	1	1.32	1.72	2.02	1.45
Y (m)	1	0.5	0.4	1	1.16	1	1	1	1.25

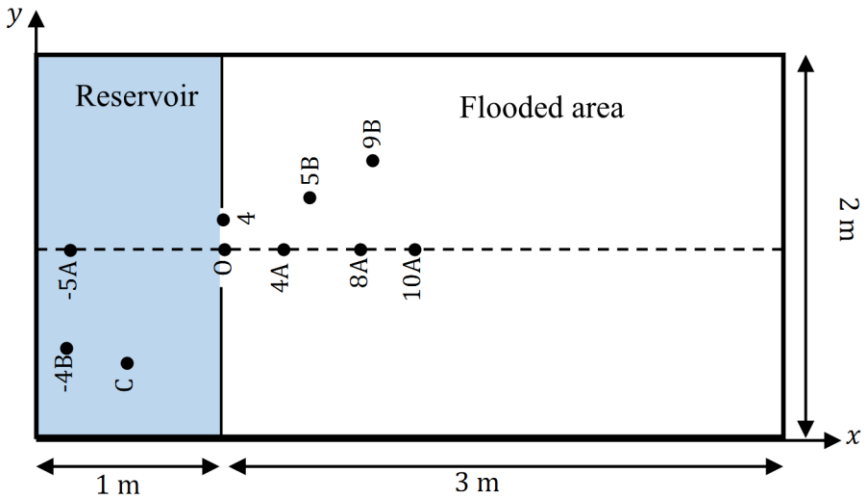


Figure 3. Plan view of the partial Dambreak experimental setup

2.3.3 Dambreak in a Venturi Channel

This test case, originally proposed by Franco (1996), involves an unsteady Dambreak flow in a channel with a convergent-divergent (Venturi) contraction. It is specifically designed to assess the model's capability to handle complex 2D flows in variable-width domains, including the coexistence of subcritical and supercritical flow regimes, shock wave generation, and partial wave reflection.

The channel is rectangular and horizontal, with a total length of 19.3 m and a nominal width of 0.5 m (Figure 4). A dam is positioned 6.1 m from the upstream end. At 7.7 m downstream of the dam, the channel contracts linearly over a length of 1.0 m to a minimum throat width of 0.1 m, after which it expands symmetrically back to its original width. The initial water depth is 0.3 m upstream of the dam and 0.003 m downstream, representing a near-dry bed condition. A closed-wall boundary condition is imposed at the upstream end and a transmissive (open) condition at the downstream end. The Manning roughness coefficient is $n = 0.01$ m$^{-1/3}$s.

Four gauge points (G1–G4) are located along the channel centreline (Table 3). G1, situated upstream of the dam, records the arrival of the rarefaction wave and the subsequent drop in water depth. G2, located upstream of the contraction, captures the initial shock wave arriving at approximately $t = 3$ s, followed at $t \approx 7.3$ s by a second abrupt depth change associated with a reflected shock propagating upstream from the contraction. G3 is positioned within the throat

and records the sudden depth increase caused by the local contraction. G4 lies downstream of the contraction and registers a weaker, diffracted shock before the flow progressively reaches a quasi-steady state.

Table 3. Coordinates of gauge points for the Venturi channel test case.

Gauge	G1	G2	G3	G4
X (m)	0.25	0.25	0.25	0.25
Y (m)	5.1	12.2	14.7	16.6

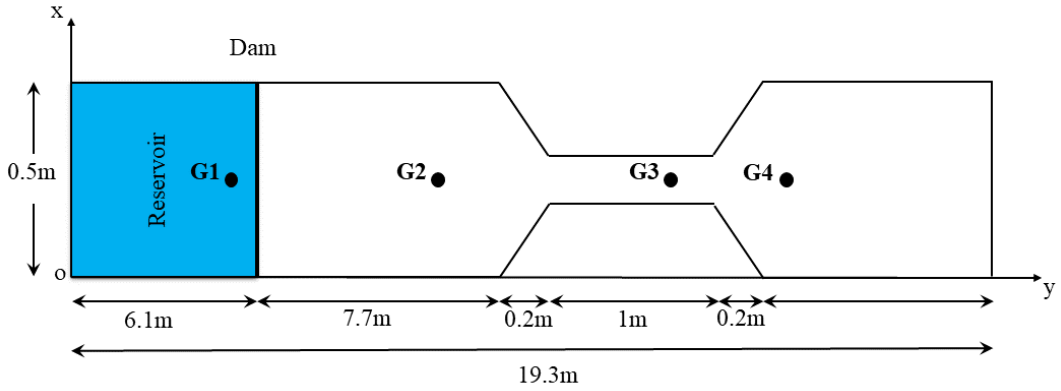


Figure 4. Plan view geometry of the Venturi channel.

3. Results and Discussion

For each test case, the computed water depths and velocities are compared against analytical solutions or experimental measurements, and error metrics are analysed to assess the relative performance of the PINNS model.

3.1 Test 1. 1D Typical Dambreak

The dam, initially placed at the midpoint of the channel, collapses instantaneously at t = 0 s. Analysis of the Froude number (Figure 5) confirms the coexistence of subcritical flow in the wet-bed case and supercritical flow in the dry-bed case along the channel. The Dambreak event generates two distinct wave structures in the wet-bed scenario: a rapidly propagating shock wave travelling downstream and a rarefaction wave propagating upstream. In the dry-bed case, only a single rarefaction wave is produced.

The spatial profiles of water depth and specific discharge confirm that the PINNs model correctly tracks the wave-front celerity and preserves the correct jump conditions across the shock. The Froude number distributions illustrated in Figure 5 are faithfully reproduced for both the subcritical wet-bed regime and the supercritical dry-bed regime. Figure 6 and Figure 7 present the numerical results of both methods at t = 3 s after dam failure illustrating the spatial evolution of water depth and the velocity for wet and dry bed respectively.

Quantitatively, the MAE for water depth remains below 0.27% in both cases (Table 4), which represents excellent agreement with the analytical solution. The comparatively higher velocity RMSE in the dry-bed case (0.805) is a well-documented consequence of the singularity in the velocity field at the advancing wet–dry front, where the denominator in the velocity computation approaches zero; this artefact does not undermine the overall quality of the free-surface prediction.

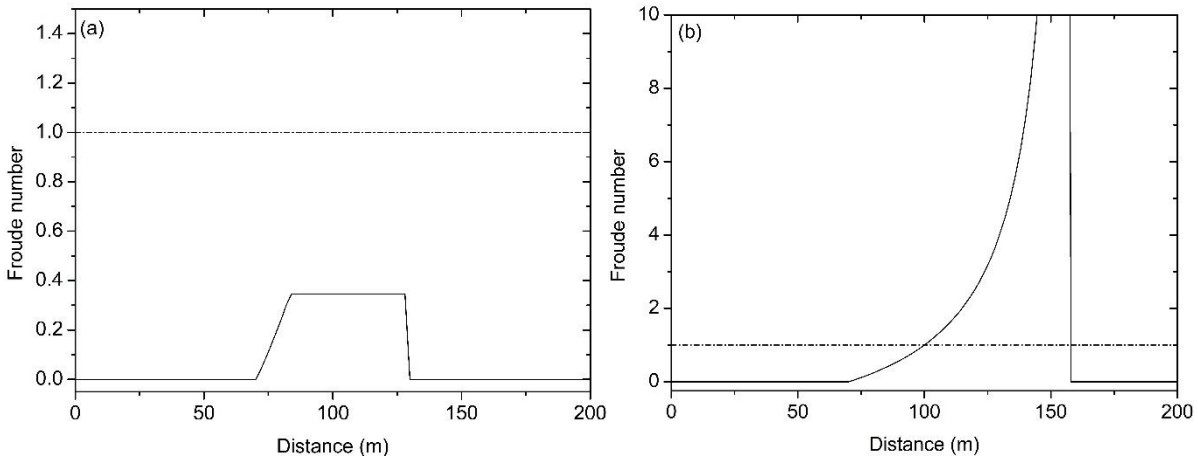


Figure 5. Froude number variation for both flow regimes: (a) wet bed (subcritical case) (b) dry bed (supercritical case).

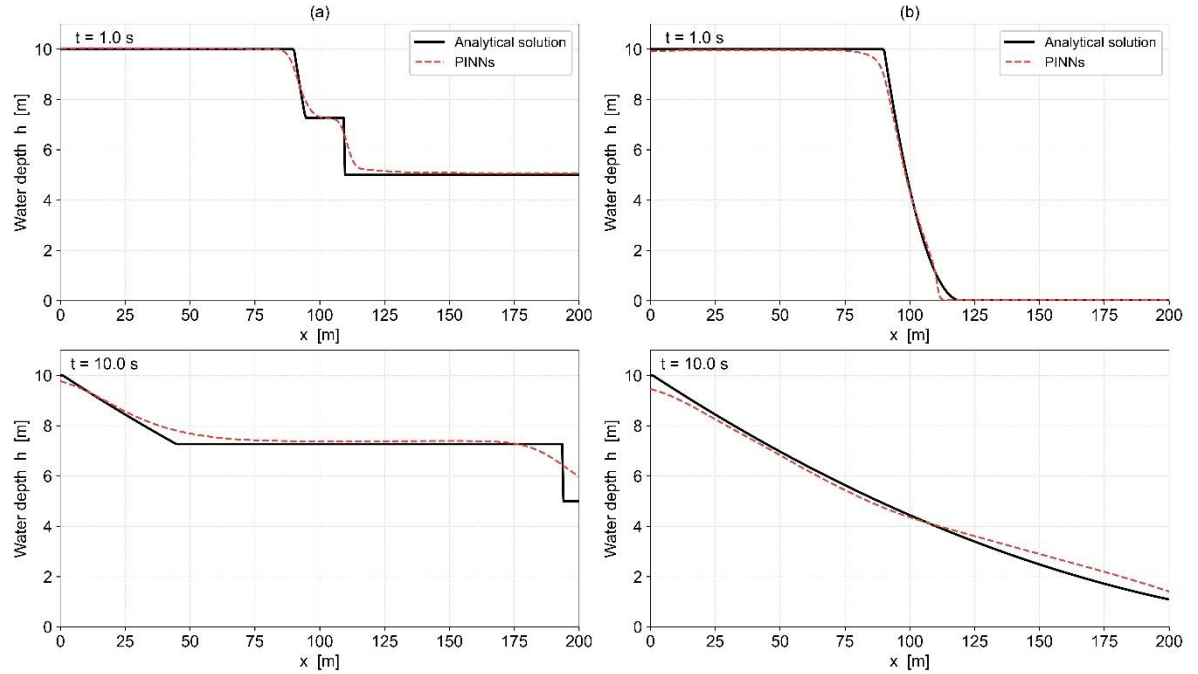


Figure 6. Comparative water depth results for the typical 1D Dambreak (a) Wet bed (b) Dry bed

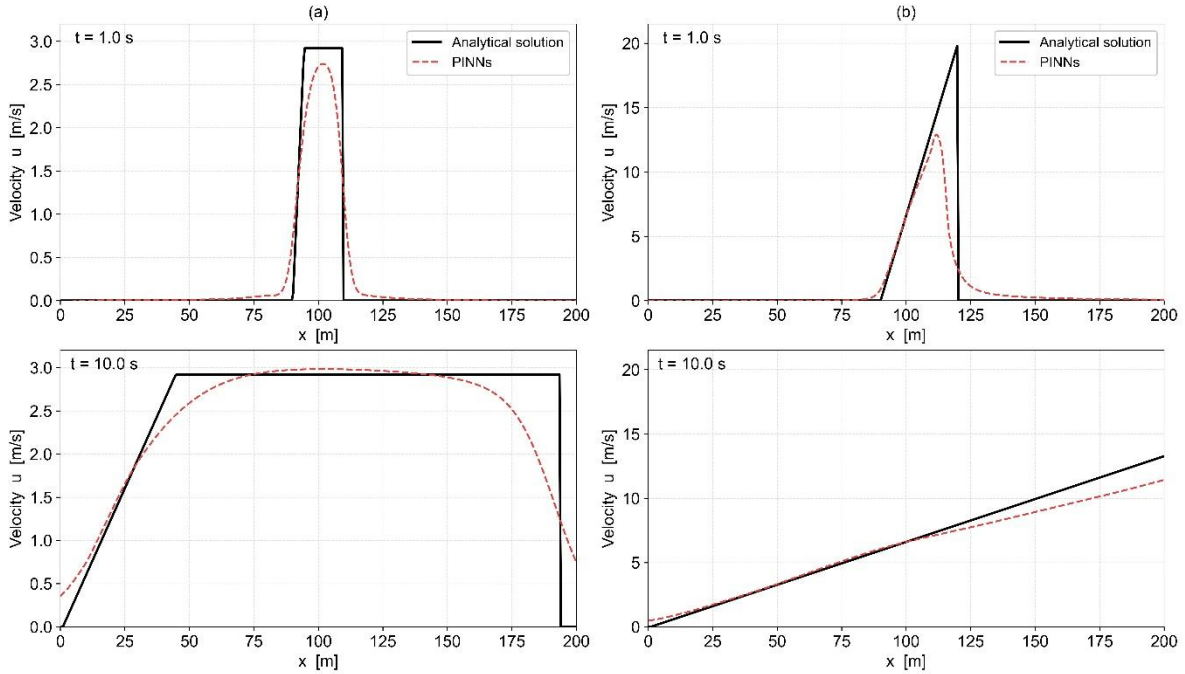


Figure 7. Comparative velocity results for the typical 1D Dambreak (a) Wet bed (b) Dry bed

PINNs method reproduce the shock wave with good accuracy. The relative error metrics reported in Table 4 quantify this agreement using the L2 relative error norm and the mean absolute error :

$$\boldsymbol{E_{L2}} = \sqrt{\frac{\sum(\boldsymbol{h_a} - \boldsymbol{h_c})^2}{\boldsymbol{h_a}^2}} \tag{15}$$

$$\mathbf{MAE} = \frac{\mathbf{1}}{\boldsymbol{n}} \sum |\boldsymbol{h_a} - \boldsymbol{h_c}| \tag{14}$$

where h_a denotes the analytical water depth, h_c is the calculated depth, and n is the total number of time steps.

Table 4. RMSE and MAE for the typical 1D Dambreak (wet and dry cases).

	Wet Case		Dry Case	
	MAE (%)	RMSE	MAE (%)	RMSE
h (m)	0.2119	0.3090	0.2632	0.2970
u (m/s)	0.2196	0.3902	0.5646	0.8053

The MAE values for water depth remain below 0.27% in both cases, confirming that both schemes achieve satisfactory accuracy for the free-surface profile. The higher velocity errors observed in the dry-bed case (MAE = 0.565%, RMSE = 0.805) are physically expected: the dry-bed wave front involves a sharper, moving wet–dry interface, a well-known challenge for numerical solvers, where the velocity field transitions abruptly from rest.

3.2 Test 2. 1D Dambreak over a Triangular Bump

The instantaneous and total dam failure at t = 0 s initially generates an expansion wave propagating upstream and a shock wave travelling rapidly along the channel. Downstream of the triangular obstacle, the flow dynamics become considerably more complex, involving

multiple wave interactions. Figure 8 compares the predicted and observed water depths at several measurement gauge stations.

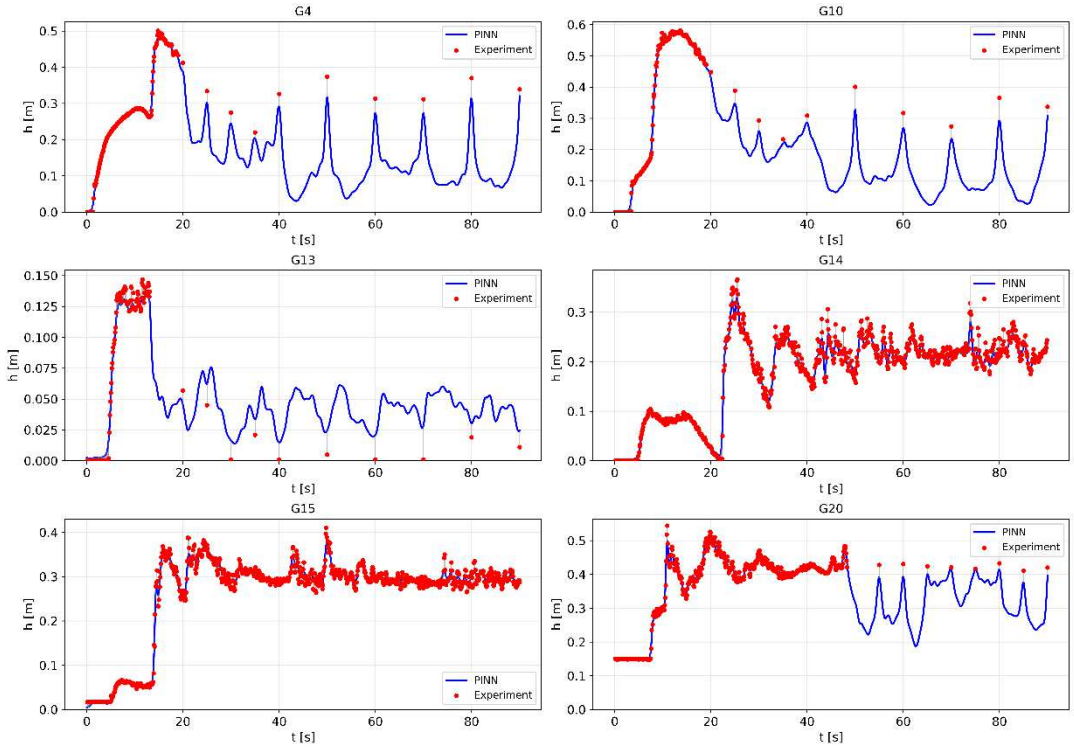


Figure 8. Computed and observed water depth time series at gauge stations.

The quantitative error metrics are reported in Table 5. The high R^2 values across all gauges (0.982–0.997) confirm that both methods capture the dominant temporal wave dynamics with high fidelity. The global RMSE of 0.00994 m and MAE of 0.00663 m fall well within the range of acceptable accuracy for shallow-water modelling.

Table 5. Error metrics for the 1D Dambreak over a triangular bump.

Gauge	RMSE [m]	L2 [%]	MAE [m]	Max Err [m]	R^2
G4	0.009765	3.1146	0.004646	0.055109	0.9947
G10	0.012767	3.0966	0.007340	0.071556	0.9968
G13	0.007429	7.6236	0.005606	0.027332	0.9855
G14	0.011033	5.6267	0.007714	0.054857	0.9817
G15	0.009140	3.2540	0.006363	0.050239	0.9912
G20	0.008538	2.2042	0.005933	0.043077	0.9934
Global	0.009941	3.4570	0.006627	0.071556	0.9947

The elevated L2 error at gauge G13 (7.62%) reflects its position at the obstacle crest, where flow transitions sharply between subcritical and supercritical regimes. The model also underestimates water depth at G14. A non-physical depth oscillation near the closed downstream boundary appears at $t = 5.4$ s but dissipates by $t = 7.4$ s at gauge G20. Overall, the PINNs model captures the arrival time, amplitude, and recession limb of the primary wave at gauges G4, G10, G15, and G20 ($R^2 = 0.991$–0.997), and the global RMSE of 0.00994 m with $R^2 = 0.9947$ confirms high-fidelity resolution of this multi-wave interaction scenario (Figure 9).

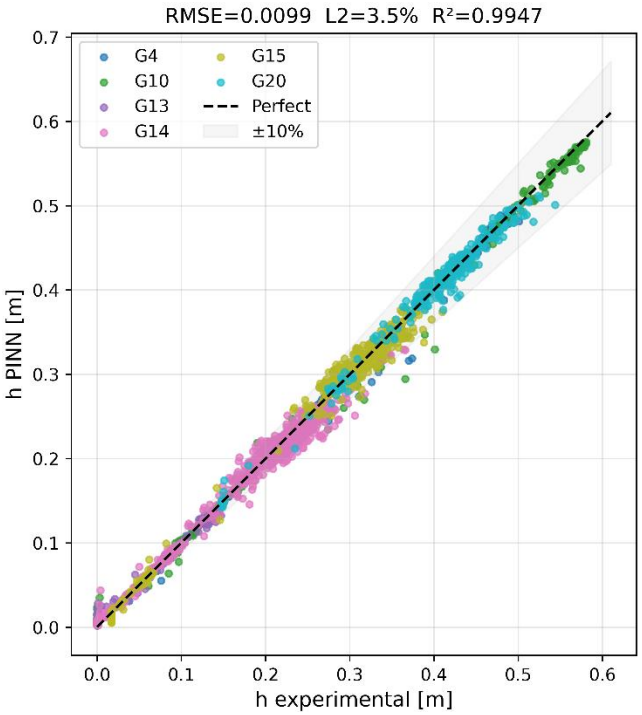


Figure 9. Scatter plot of PINN-predicted versus experimental water depth for different gauge stations

3.3 Test 3. 2D Partial Dambreak

Figure 10 compares the simulated and measured water depths at the observation points 10 seconds after the partial dam break. In general, the PINNs formulation reproduces the free-surface elevations satisfactorily at all gauge stations, and the overall agreement between the computed and experimental results is considered good. The error metrics reported in Table 6 confirm this assessment quantitatively.

Table 6. RMSE, MAE, Maximum Error, and R^2 at gauge stations.

Gauge	RMSE [m]	L2 [%]	MAE [m]	Max Err [m]	R^2
C	0.005731	1.8392	0.005012	0.009519	0.9984
O	0.010904	3.0221	0.010459	0.015646	0.9955
H4	0.013738	4.3689	0.011241	0.028084	0.9912
4A	0.010681	8.2504	0.007162	0.026180	0.9866
8A	0.004021	5.1162	0.003421	0.008323	0.9944
10A	0.002446	5.9511	0.002148	0.004108	0.9899
Global	0.009459	3.6024	0.007184	0.028084	0.9969

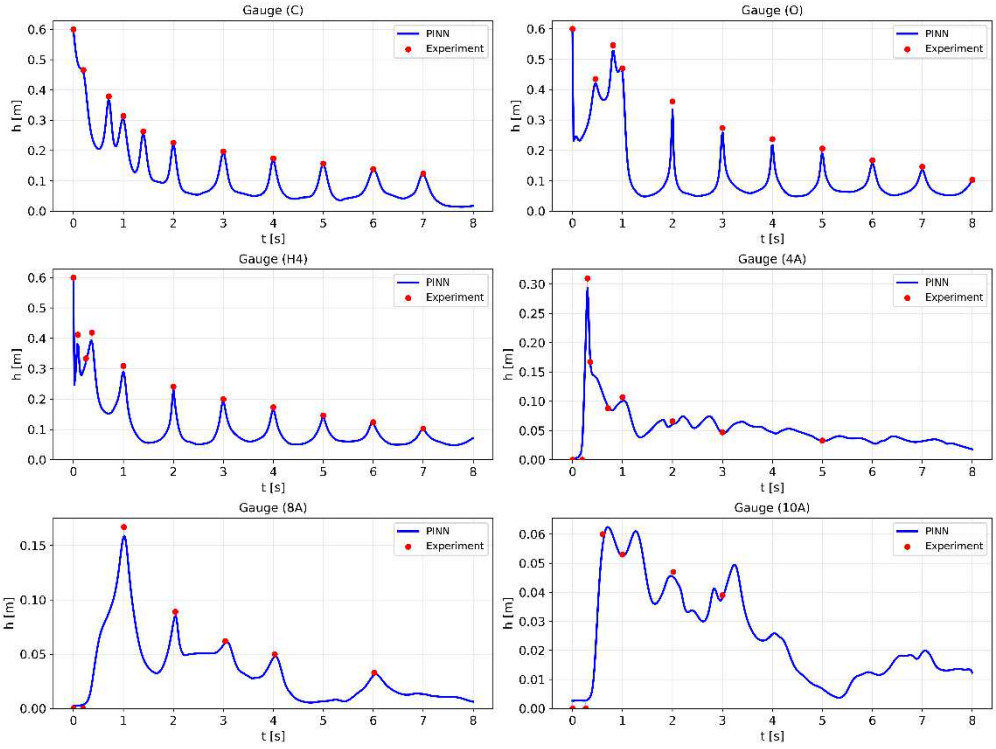


Figure 10. Computed vs. measured water depths at observation points

The largest relative error occurs at gauge 4A (L2 = 8.25%), located in the highly dynamic zone just downstream of the breach where strong lateral jet expansion and transverse velocity gradients create near-3D flow that a depth-averaged model cannot fully resolve. Gauges 8A and 10A, located further downstream, show MAE below 0.003 m, confirming accurate prediction of far-field wave propagation and flood attenuation over the initially dry bed. The global R^2 of 0.9969 and RMSE of 0.00946 m establish the PINNs model as a reliable predictor for 2D partial-breach scenarios (Figure 11).

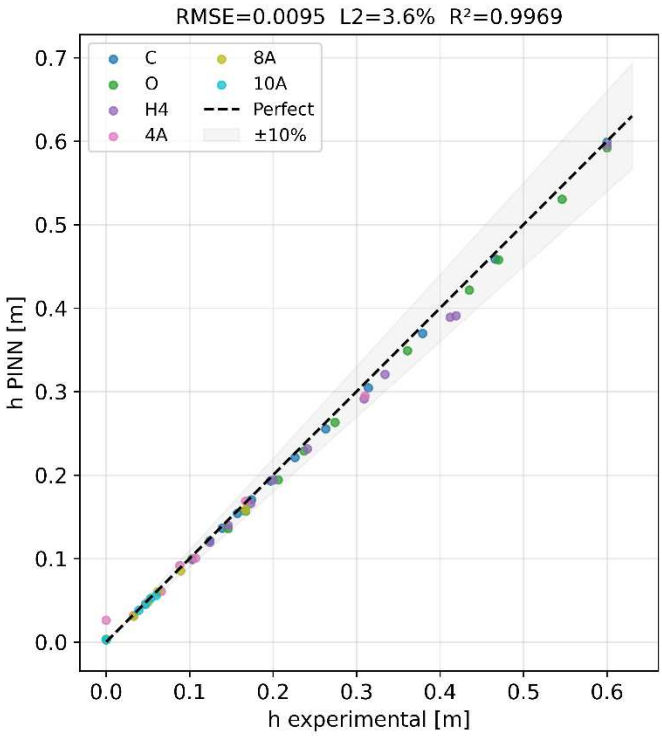


Figure 11. Scatter plot of PINN-predicted versus experimental water depth for different gauge stations

3.4 Test 4. 2D Dambreak in a Venturi Channel

Figure 12 compares the experimental data and the numerical results for the temporal evolution of water depth at measurement points G1, G2, G3, and G4. The relative L2 errors are reported in Table 7. The PINNs approach produces notably superior results according to this metric, particularly at the gauges most influenced by the channel contraction.

Table 7. RMSE, MAE, Maximum Error, and R^2 at gauge stations.

Gauge	x	y	RMSE	L2%	MAE	Max Err	R^2
G1	0.48	0.40	0.00080	0.47	0.00062	0.00295	0.9997
G2	1.00	1.00	0.00351	3.08	0.00203	0.01872	0.9981
G3	1.00	1.16	0.00271	3.59	0.00156	0.01296	0.9969
G4	1.32	1.00	0.00201	12.29	0.00113	0.01022	0.9642
Global			0.00247	2.24	0.00133	0.01872	0.9990

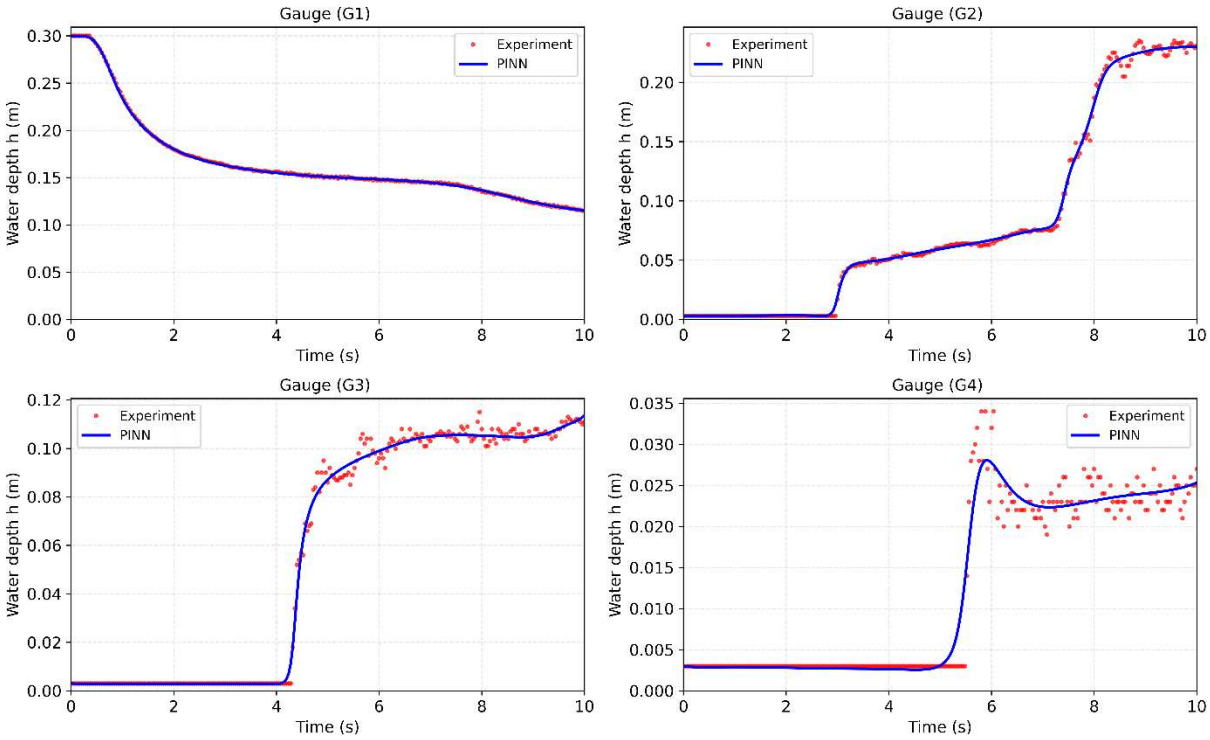


Figure 12. PINN's predicted vs. measured water depths at observation points.

The numerical solutions generated by the PINNs model satisfactorily reproduce the physical behavior of the Dambreak wave, despite minor discrepancies relative to the observed data at gauges G1 and G3 (Figure 12). The training loss history of the PINNs model, characterized by oscillatory convergence over 20,000 epochs with a reduction of two to three orders of magnitude across all loss components, reflects the multi-objective, non-convex nature of the physics-informed optimization problem, further amplified by the adaptive collocation resampling strategy employed every 5,000 Adam iterations. Despite these fluctuations, the consistent convergence trend confirms that the network successfully balances data fidelity and physical consistency constraints. This translates into superior L2 accuracy in the Venturi test, where the constricted geometry and strong pressure gradients challenge conventional numerical schemes but are naturally handled by the continuous representation of the neural network solution.

Taken together, the four test cases demonstrate that the PINNs model is robust across a spectrum of flow regimes and geometric configurations. The error metrics consistently remain within acceptable engineering tolerances, and the high R^2 values (0.982–0.997) across all gauges and configurations confirm strong predictive capability (Figure 13). The model's most significant advantage over classical mesh-based solvers lies in its ability to embed the governing shallow-water equations directly into the loss function, ensuring physical consistency without requiring explicit discretisation of the spatial or temporal domain. This property is particularly beneficial in irregular geometries such as the Venturi channel and near complex boundary conditions such as those encountered in the partial Dambreak scenario.

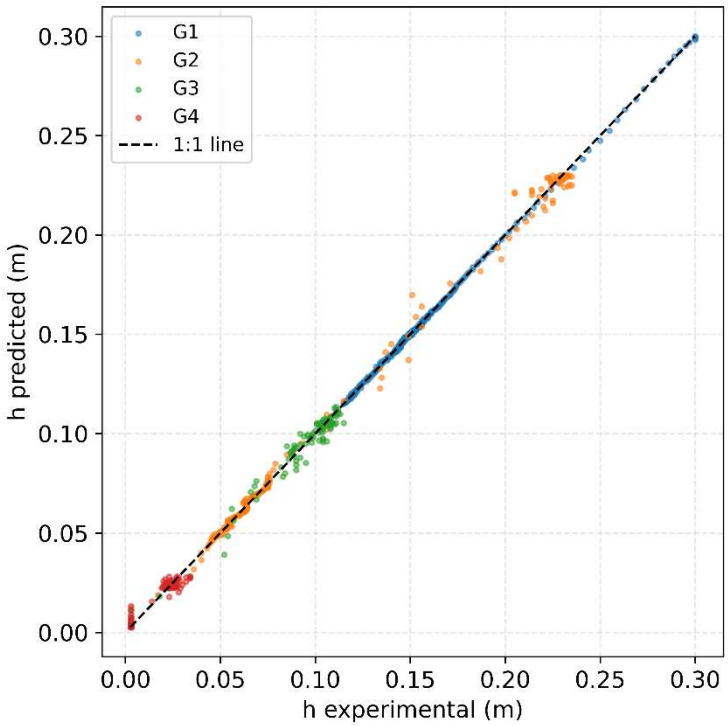


Figure 13. Scatter plot of PINN-predicted versus experimental water depth for different gauge points

4. Conclusion

This paper presented and evaluated a unified Physics-Informed Neural Network (PINN) framework for dam-break flows governed by the shallow water equations (SWEs). Four benchmark cases of increasing complexity, a canonical 1D dam-break, a 1D dam-break over a triangular obstacle, a 2D partial dam-break, and a 2D dam-break in a Venturi channel, provided a rigorous test of the framework's accuracy, robustness, and physical consistency.

The PINNs model achieves consistently high accuracy across all configurations: global R^2 between 0.982 and 0.997, RMSE below 0.01 m, and L2 errors well within engineering tolerances in smooth flow regions. It correctly reproduces shock wave propagation, rarefaction fan structure, wet–dry front advancement, obstacle-induced wave interactions, lateral jet expansion, and flow acceleration through channel contractions. Taken together, these results confirm that physics-informed learning can serve as a reliable surrogate for classical finite-volume solvers in complex shallow-water problems.

Four practical advantages stand out. First, the mesh-free formulation removes the need for grid generation, which is particularly valuable for irregular geometries like the Venturi channel. Second, embedding the continuity and momentum equations in the loss function enforces physical consistency throughout the domain, no upwinding, Riemann solvers, or flux limiters are needed. Third, the network delivers smooth, differentiable solution fields suited for post-processing applications such as flood hazard mapping or sensitivity analysis. Fourth, once trained, the model evaluates solutions at arbitrary query points without re-running the full system.

The study also identifies clear limitations. Training is expensive: the non-convex, multi-objective optimisation requires up to 20,000 epochs and remains sensitive to architecture,

learning rate, and collocation point distribution. Even with adaptive resampling, training time exceeds a single forward pass of a well-optimised FVM solver at comparable resolution. Sharp-gradient regions, the wet–dry interface in Test 1, gauges G13 and 4A in Tests 2–3, still produce elevated errors that point to the difficulty of representing discontinuities in a single smooth network. Domain decomposition, hp-adaptive architectures, and hybrid PINN–FVM coupling are promising directions. The depth-averaged assumption also limits applicability near the breach, where vertical accelerations are non-negligible. Extending the framework to non-hydrostatic or 3D formulations, and testing it against real-world digital elevation models under uncertain boundary conditions, are open questions for future work.

PINNs offer a physically grounded, mesh-free path for simulating dam-break flows that achieves engineering-grade accuracy across both 1D and 2D configurations with wet and dry beds, obstacles, partial breaches, and channel contractions. The approach is especially well-suited to geometrically complex domains and far-field wave prediction. Addressing the training cost and sharp-gradient resolution through more advanced optimisation strategies and adaptive architectures, and eventually coupling with established solvers, will be the focus of future work, with the goal of making PINN-based models viable in operational flood forecasting.

Author Contributions Conceptualization: Zakaria Mahfoud; Formal analysis and investigation: Nureddine Maref; Writing – original draft preparation: Abdelkader Bemmoussat; Supervision, Writing – review and editing: Khaled Korichi.

Data Availability Statement The data will be made available upon request.

Funding Statement This research received no specific grant from any funding agency in the public, commercial, or not-for-profit sectors.

Conflict of Interest The authors declare there is no conflict of interest.

Ethics Approval and Consent to Participate Not applicable.

Acknowledgments Not applicable.

References

Bates, P. D., Horritt, M. S., & Fewtrell, T. J. (2010). A simple inertial formulation of the shallow water equations for efficient two-dimensional flood inundation modelling. *Journal of Hydrology*, *387*(1), 33–45. https://doi.org/https://doi.org/10.1016/j.jhydrol.2010.03.027

Baydin, A. G., Pearlmutter, B. A., Radul, A. A., & Siskind, J. M. (2018). Automatic differentiation in machine learning: A survey. *Journal of Machine Learning Research*, *18*.

Bermúdez, M., Cea, L., & Sopelana, J. (2019). Quantifying the role of individual flood drivers and their correlations in flooding of coastal river reaches. *Stochastic Environmental Research and Risk Assessment*, *33*(10), 1851–1861. https://doi.org/10.1007/s00477-019-01733-8

Bihlo, A., & Popovych, R. O. (2022). Physics-informed neural networks for the shallow-water equations on the sphere. *J. Comput. Phys.*, *456*(C). https://doi.org/10.1016/j.jcp.2022.111024

Brunner, G. W. (2016). HEC-RAS river analysis system user's manual version 5.0. *US Army Corps of Engineers*, *962*.

Cai, S., Mao, Z., Wang, Z., Yin, M., & Karniadakis, G. (2022). Physics-informed neural networks (PINNs) for fluid mechanics: a review. *Acta Mechanica Sinica*, *37*. https://doi.org/10.1007/s10409-021-01148-1

Cedillo, S., Núñez, A.-G., Sánchez-Cordero, E., Timbe, L., Samaniego, E., & Alvarado, A.

(2022). Physics-Informed Neural Network water surface predictability for 1D steady-state open channel cases with different flow types and complex bed profile shapes. *Advanced Modeling and Simulation in Engineering Sciences*, *9*(1), 10. https://doi.org/10.1186/s40323-022-00226-8

Chen, Y., Lu, L., Karniadakis, G., & Negro, L. (2020). Physics-informed neural networks for inverse problems in nano-optics and metamaterials. *Optics Express*, *28*, 11618–11633. https://doi.org/10.1364/OE.384875

Dazzi, S. (2024). Physics-Informed Neural Networks for the Augmented System of Shallow Water Equations With Topography. *Water Resources Research*, *60*. https://doi.org/10.1029/2023WR036589

Feng, D., Tan, Z., & He, Q. (2023). Physics-Informed Neural Networks of the Saint-Venant Equations for Downscaling a Large-Scale River Model. *Water Resources Research*, *59*(2), e2022WR033168. https://doi.org/https://doi.org/10.1029/2022WR033168

Fraccarollo, L., & Toro, E. F. (1995). Experimental and numerical assessment of the shallow water model for two-dimensional dam-break type problems. *Journal of Hydraulic Research*, *33*(6), 843–864. https://doi.org/10.1080/00221689509498555

Franco, A. B. (1996). *Modelação computacional e experimental de escoamentos provocados pela rotura de barragens*. Instituto Superior Técnico, Universidade Técnica de Lisboa.

Gallardo, J. M., Parés, C., & Castro, M. (2007). On a well-balanced high-order finite volume scheme for shallow water equations with topography and dry areas. *Journal of Computational Physics*, *227*(1), 574–601.

Guo, Z., Leitão, J. P., Simões, N. E., & Moosavi, V. (2021). Data-driven flood emulation: Speeding up urban flood predictions by deep convolutional neural networks. *Journal of Flood Risk Management*, *14*(1), e12684. https://doi.org/https://doi.org/10.1111/jfr3.12684

Harten, A., Lax, P. D., & Leer, B. van. (1983). On Upstream Differencing and Godunov-Type Schemes for Hyperbolic Conservation Laws. *SIAM Review*, *25*(1), 35–61. https://doi.org/10.1137/1025002

Hu, R., Fang, F., Pain, C. C., & Navon, I. M. (2019). Rapid spatio-temporal flood prediction and uncertainty quantification using a deep learning method. *Journal of Hydrology*, *575*, 911–920. https://doi.org/https://doi.org/10.1016/j.jhydrol.2019.05.087

Jagtap, A. D., Kharazmi, E., & Karniadakis, G. E. (2020). Conservative physics-informed neural networks on discrete domains for conservation laws: Applications to forward and inverse problems. *Computer Methods in Applied Mechanics and Engineering*, *365*, 113028. https://doi.org/https://doi.org/10.1016/j.cma.2020.113028

Kabir, S., Patidar, S., Xia, X., Liang, Q., Neal, J. C., & Pender, G. (2020). A deep convolutional neural network for rapid fluvial flood inundation modelling. *CoRR*, *abs/2006.11555*. https://arxiv.org/abs/2006.11555

Karniadakis, G. E., Kevrekidis, I. G., Lu, L., Perdikaris, P., Wang, S., & Yang, L. (2021). Physics-informed machine learning. *Nature Reviews Physics*, *3*(6), 422–440. https://doi.org/10.1038/s42254-021-00314-5

Kingma, D., & Ba, J. (2014). Adam: A Method for Stochastic Optimization. *International Conference on Learning Representations*.

Leiteritz, R., Hurler, M., & Pflüger, D. (2021). Learning Free-Surface Flow with Physics-Informed Neural Networks. *2021 20th IEEE International Conference on Machine Learning and Applications (ICMLA)*, 1668–1673. https://doi.org/10.1109/ICMLA52953.2021.00266

LeVeque, R. J. (2002). Finite Volume Methods for Hyperbolic Problems. In *Cambridge Texts in Applied Mathematics*. Cambridge University Press. https://doi.org/DOI: 10.1017/CBO9780511791253

Meng, X., Li, Z., Zhang, D., & Karniadakis, G. E. (2019). PPINN: Parareal Physics-Informed Neural Network for time-dependent PDEs. *ArXiv*, *abs/1909.10145*. https://api.semanticscholar.org/CorpusID:202718994

Morris, M. (2000). *CADAM: Concerted Action on Dambreak Modelling*.

Mosavi, A., Ozturk, P., & Chau, K. (2018). Flood Prediction Using Machine Learning Models: Literature Review. *Water*, *10*(11). https://doi.org/10.3390/w10111536

Nascimento, R. G., Fricke, K., & Viana, F. A. C. (2020). A tutorial on solving ordinary differential equations using Python and hybrid physics-informed neural network. *Engineering Applications of Artificial Intelligence*, *96*, 103996. https://doi.org/https://doi.org/10.1016/j.engappai.2020.103996

Qi, X., De Almeida, G., & Maldonado, S. (2023). *Physics informed neural networks for solving flow problems modeled by the Shallow Water Equations*. https://doi.org/10.22541/essoar.168748449.92610562/v1

Raissi, M., Perdikaris, P., & Karniadakis, G. E. (2019). Physics-informed neural networks: A deep learning framework for solving forward and inverse problems involving nonlinear partial differential equations. *Journal of Computational Physics*, *378*, 686–707. https://doi.org/https://doi.org/10.1016/j.jcp.2018.10.045

Roe, P. L. (1981). Approximate Riemann solvers, parameter vectors, and difference schemes. *Journal of Computational Physics*, *43*(2), 357–372. https://doi.org/https://doi.org/10.1016/0021-9991(81)90128-5

Solomatine, D. P., & Ostfeld, A. (2008). Data-driven modelling: some past experiences and new approaches. *Journal of Hydroinformatics*, *10*(1), 3–22. https://doi.org/10.2166/hydro.2008.015

Strikwerda, J. C. (2004). *Finite Difference Schemes and Partial Differential Equations, Second Edition*. Society for Industrial and Applied Mathematics. https://doi.org/10.1137/1.9780898717938

Tartakovsky, A. M., Marrero, C. O., Perdikaris, P., Tartakovsky, G. D., & Barajas-Solano, D. (2020). Physics-Informed Deep Neural Networks for Learning Parameters and Constitutive Relationships in Subsurface Flow Problems. *Water Resources Research*, *56*(5), e2019WR026731. https://doi.org/https://doi.org/10.1029/2019WR026731

Thompson, J. F., Soni, B. K., & Weatherill, N. P. (1998). *Handbook of grid generation*. CRC press.

Tian, Y., Ding, S., Huang, L., Su, G., & Chen, J. (2025). Physics-Informed Neural Networks for Solving the Two-Dimensional Shallow Water Equations With Terrain Topography and Rainfall Source Terms. *Water Resources Research*, *61*(9), e2025WR040052. https://doi.org/https://doi.org/10.1029/2025WR040052

Toro, E. F. (2001). Shock-Capturing Methods for Free-Surface Shallow Flows. In J. W. S. Ltd (Ed.), *Chichester etc Wiley*. John Wiley & Sons. http://scholar.google.com/scholar?hl=en&btnG=Search&q=intitle:Shock-Capturing+Methods+for+Free-Surface+Shallow+Flows#0

Toro, E. F., Spruce, M., & Speares, W. (1994). Restoration of the contact surface in the HLL-Riemann solver. *Shock Waves*, *4*(1), 25–34. https://doi.org/10.1007/BF01414629

Vreugdenhil, C. B. (2013). *Numerical methods for shallow-water flow* (Vol. 13). Springer Science \& Business Media.

Xu, K., & Darve, E. (2019). *Adversarial Numerical Analysis for Inverse Problems*. https://doi.org/10.48550/arXiv.1910.06936

Zhang, D., Guo, L., & Karniadakis, G. E. (2020). Learning in Modal Space: Solving Time-Dependent Stochastic PDEs Using Physics-Informed Neural Networks. *SIAM Journal on Scientific Computing*, *42*(2), A639–A665. https://doi.org/10.1137/19M1260141

Zienkiewicz, O. C., & Taylor, R. L. (2005). *The finite element method set*. Elsevier.